

## Systematic investigation of relativistic effects in EXAFS data analysis

Georghii Tchoudinov <sup>1</sup>, Andrea Di Cicco,<sup>1</sup> and Calogero R. Natoli <sup>2</sup>

<sup>1</sup>*Physics Division, School of Science and Technology, Università di Camerino, Italy*

<sup>2</sup>*INFN Laboratori Nazionali di Frascati, c.p. 13, I-00044 Frascati, Italy*



(Received 17 November 2021; accepted 16 March 2022; published 28 April 2022)

Modern XAFS (x-ray absorption fine structure) data analysis is based on accurate multiple-scattering (MS) calculations of the x-ray absorption cross section, usually carried out solving the nonrelativistic Schrödinger equation for complex effective optical muffin-tin potentials describing the scattering of the atoms. The introduction of relativistic effects in extended XAFS (EXAFS) multiple-scattering calculations has been described in several papers and shown to be important for heavy atoms. However, few examples of applications and detailed studies of relativistic effects were given so far. In this work, we have performed a systematic investigation of relativistic corrections in systems of increasing atomic number, using a reliable simulation scheme recently developed and based on the incorporation of a pseudo-Schrödinger equation effectively replacing the Dirac relativistic form. Calculations have been put to a test in 12 different pure-element condensed-state systems, with the atomic number ranging from  $Z = 10$  for crystalline Ne to  $Z = 90$  for crystalline Th. The importance of accounting for relativistic effects has been highlighted for elements with  $Z \gtrsim 60$ , as ones for which relativistic corrections for amplitudes of calculated XAFS MS signals exceed 10%. The size of relativistic effects for calculated higher-order XAFS signal (with respect to the dominant single-scattering first-neighbor signal) has been shown, taking as example the  $L_3$ -edge spectra of crystalline Au and Pb. The size of relativistic effects for the  $K$  and  $L_3$  edges has been also evaluated, showing a slight increase of relativistic corrections for the  $L_3$  edge. The improvement in the accuracy of XAFS simulations has been demonstrated comparing the results obtained for structural refinements of the  $L_3$  edge of crystalline Au at 300 K.

DOI: [10.1103/PhysRevB.105.144109](https://doi.org/10.1103/PhysRevB.105.144109)

### I. INTRODUCTION

The x-ray absorption spectroscopy (XAS) is a modern experimental technique allowing fine analysis of structural and electronic properties of a given atomic, molecular, or condensed system [1,2]. Information about the electronic and local structure is mainly associated with the oscillations of the x-ray absorption cross section following selected core-level edges. This technique became very popular in the last 30 years due to the increasing availability of synchrotron radiation sources, and the interpretation of the so-called XAFS (x-ray absorption fine structure) or EXAFS (extended XAFS) patterns were continuously improved by progresses in theoretical and computational tools.

In fact, the interpretation of the measured XAS signals required the development of suitable advances in theoretical approaches and complex calculation schemes based mostly on the multiple-scattering (MS) theory. In this approach, the absorption cross section can be calculated as a one-electron photoexcitation process in which the photoelectron interacts with a collection of (spherical) potentials. The model calculations can be performed using atomic clusters of limited size, due to the strong interaction of the photoelectron with the surrounding matter at the typical kinetic energies under consideration, leading to a finite mean-free path of the electron probe. The XAFS technique, especially for high kinetic energies, is thus sensitive to the local structure of the given atomic system.

Several MS methods have been developed for performing XAFS data analysis [1]. In particular, the GNXAS package implements state-of-the-art methods for the computation of XAFS signal [2–4] in the framework of the multiple-scattering (MS) theory, using a complex effective optical potential for the photoelectron moving in a cluster of atoms modeling the system under study. The XAFS signal so obtained constitutes the input for a rigorous fitting procedure to the raw experimental data in order to derive structural information on the system. The underlying theory, basic methodology, and practical applications have been widely discussed elsewhere (see, for example, [3–6] and references therein).

One of the present limitations of many XAFS data-analysis methods is the use of the nonrelativistic Schrödinger equation which may prevent accurate XAFS data analysis when atoms with high atomic number  $Z$  are involved in the system under study. The importance and possible introduction of relativistic effects in XAFS multiple-scattering calculations has been described in some previous works (see [7,8] for example). Relativistic effects are included in the current distributions of the FEFF XAFS data-analysis software [9], but to our knowledge no detailed studies of the relevance of relativistic corrections in different systems have been published so far.

The purpose of this work is to present a systematic study on the relevance of relativistic effects for different atomic structures. This task has been carried out introducing relativistic corrections within the GNXAS suite of programs. As briefly

described in a recent work [10], the introduction of relativistic corrections is realized by modifying the program (PHAGEN, part of the GNXAS suite [4,11]) that generates atomic absorption cross sections and scattering  $t$  matrices for the selected cluster defining the phase shifts for each angular momentum. This goal is made possible by deriving a pseudo-Schrödinger equation from the Dirac equations that takes into account all the relevant relativistic corrections.

Here, model XAFS relativistic and nonrelativistic MS calculations are performed for different systems changing the involved core levels by increasing the atomic number of the photoabsorbing species (typically from  $Z = 10$  to 90). The scattering  $t$  matrices defining the phase shifts'  $\delta_l$  functions, as well as the amplitude and phase of typical MS signals associated with the selected atomic systems, are calculated with the aim of comparing nonrelativistic and relativistic approximations in a wide range. The final goal is obtaining accurate information about the magnitude of relativistic effects for increasing atomic numbers, determining the conditions for which XAFS data analysis should be performed accounting for those effects. A practical example showing the application of relativistic and nonrelativistic calculations to the XAFS data analysis of crystalline gold is here reported as well.

This paper is organized as follows: In Sec. II we present a summary of the theory and methods used for the relativistic calculations. In Sec. III we discuss the results of our simulations for different atoms and structure covering atomic numbers in the range  $Z = 10$ –90; the results of relativistic phase-shift calculations and of amplitude and phase of the corresponding MS XAFS signals are presented, respectively, in Secs. III A and III B. An example of XAFS data analysis

of crystalline gold is discussed in Sec. III C. Section IV is devoted to the conclusions.

## II. CALCULATION METHOD

A relativistic version of the XAS formalism restricted to nonmagnetic materials has been originally developed by Tyson [7]. The construction of the multiple-scattering (MS) series, adopting the one-electron and muffin-tin approximations, leads to the standard interpretation of XAS as convergent superposition of contributions from closed paths traveled by the ejected photoelectron, probing the local environment and returning to the photoexcitation site. The choice of the complex Hedin-Lundqvist [12] potential is a standard choice for nonmagnetic materials, which efficiently accounts for inelastic losses during the photoelectron propagation.

Upper and lower Dirac components relative to the radial Dirac equations (see Appendix) are treated on the same footing in [7], and following [13,14] one gets the fully relativistic polarization-averaged XAS cross section for transitions to a dipole-selected final state of angular momentum  $j_\kappa = |\kappa| - 1/2$ ,  $\kappa$  being the eigenvalue of the operator  $(1 + 2\mathbf{s} \cdot \mathbf{l})$  relative to the spin-spherical harmonic  $\chi_\kappa^\mu(\hat{r}) \equiv \sum_{v=\pm 1} \langle l_\kappa, \mu - v, 1/2, v/2 | j_\kappa, \mu \rangle Y_{l_\kappa, \mu-v}(\hat{r}) \chi_v$  [15].

In this work the contribution of lower Dirac components has been neglected, following [16], who have shown in the context of Dirac-Hartree-Fock calculations for an atom, that the small Dirac components  $v_{n\kappa}$  account to less than 1% of the total radial electronic charge density [even in many-electron atoms for which relativistic effects are important, as the uranium ( $Z = 92$ ) one]. The total polarization-averaged XAS cross section then becomes

$$\begin{aligned} \sigma(\omega) = & -\frac{4\pi\alpha\omega}{3}(2j_{\kappa_c} + 1) \sum_{\kappa} \left[ \frac{2j_{\kappa_c} + 3}{4(j_{\kappa_c} + 1)} \delta_{j_\kappa, j_{\kappa_c} + 1} \delta_{l_\kappa, l_{\kappa_c} + 1} + \frac{1}{4j_{\kappa_c}(j_{\kappa_c} + 1)} \delta_{j_\kappa, j_{\kappa_c}} \delta_{|l_\kappa - l_{\kappa_c}|, 1} + \frac{2j_{\kappa_c} - 1}{4j_{\kappa_c}} \delta_{j_\kappa, j_{\kappa_c} - 1} \delta_{l_\kappa, l_{\kappa_c} - 1} \right] \\ & \times k \operatorname{Im} \left[ 2 \int_0^{r_c} dr r^3 g_{\kappa_c}(r) g_{\kappa}^H(kr) \int_0^r dr' (r')^3 g_{\kappa}^R(kr') g_{\kappa_c}(r') \right. \\ & \left. + \left( \int_0^{r_c} dr r^3 [g_{\kappa_c}(r) g_{\kappa}^R(kr)] \right)^2 \frac{1}{2j_{\kappa_c} + 1} \sum_{\mu} G_{\kappa\mu, \kappa\mu}^{cc}(\epsilon - \epsilon_F + i\Gamma_h) \right], \end{aligned} \quad (1)$$

where the angular part describes photoexcitation channels compatible with the electric dipole selection rules, namely,  $j_{\kappa_c} - j_\kappa = |\kappa_c| - |\kappa| = 0, \pm 1$  and  $l_{\kappa_c} + l_\kappa + 1 = (\text{even integer})$ , where  $l_\kappa = |\kappa| + (\text{sign}\{\kappa\} - 1)/2$ .  $g_{\kappa_c}(r)$  is the radial upper Dirac component of the core initial state (denoted by the subscript  $c$ ).  $g_{\kappa}^{R,H}(r)$  are regular (superscript  $R$ ) and singular (superscript  $H$ ) scattering solutions (relative to the muffin-tin potential of the photoabsorber atom with a core hole) of the second-order pseudo-Schrödinger equation for the upper Dirac component, obtained from the first-order coupled radial Dirac equations [16] (see Appendix A)

$$\begin{aligned} 0 = & \left[ \frac{d^2}{dr^2} + \epsilon - V(r) - \frac{\kappa(\kappa + 1)}{r^2} \right] u_\kappa(r) \quad (\text{nr}) \\ & + \frac{\alpha^2}{4} (\epsilon - V(r))^2 + \frac{\alpha^2}{4} B(r) \left( \frac{dV}{dr} \right) \left( \frac{d}{dr} - \frac{1}{r} \right) u_\kappa(r) \quad (\text{sr}) \\ & + \frac{\alpha^2}{4} B(r) \frac{1 + \kappa}{r} \left( \frac{dV}{dr} \right) u_\kappa(r) \quad (\text{so}). \end{aligned}$$

Here

$$u_\kappa(r) = r g_\kappa(r), \quad B(r, \epsilon) = \left(1 + \frac{\alpha^2}{4}(\epsilon - V(r))\right)^{-1} \quad (2)$$

and terms have been explicitly grouped as follows:

(i) (nr): These are the terms of the usual *nonrelativistic* radial Schrödinger equation. Indeed,  $-\frac{\kappa(\kappa+1)}{r^2}$  is the centrifugal term because of  $\kappa(\kappa+1) = l(l+1) \forall \kappa$ .

(ii) (sr): The first and the second terms under the label (sr) in Eq. (2) are, respectively, the mass and Darwin terms, and they constitute the *scalar-relativistic* correction.

(iii) (so): If one adds the *spin-orbit* term, which is the only one that depends explicitly on spin through the quantum number  $\kappa$  [see Eq. (3)], one gets the fully relativistic description

$$\kappa = \begin{cases} -l - 1 & \text{if } j = l + 1/2, \text{ sojp} \\ l & \text{if } j = l - 1/2, \text{ sojm.} \end{cases} \quad (3)$$

If one neglects the spin-orbit term, the polarization-averaged XAS cross section takes a basically nonrelativistic form, while the gross of relativistic effects (brought by the mass and Darwin terms) is taken into account [10]:

$$\begin{aligned} \sigma(\omega) = & -\frac{8\pi\alpha\omega}{3}(2l_c + 1) \sum_l \left[ \frac{l_c}{2l_c + 1} \delta_{l,l_c-1} + \frac{l_c + 1}{2l_c + 1} \delta_{l,l_c+1} \right] \\ & \times k \operatorname{Im} \left[ 2 \int_0^{r_c} dr g_{l_c}(r) r^3 g_l^H(kr) \int_0^r dr' g_l^R(kr') (r')^3 g_{l_c}(r') \right. \\ & \left. + \left[ \int_0^{r_c} dr g_{l_c}(r) r^3 g_l^R(kr) \right]^2 \frac{\sum_{m_l} G_{l m_l, l m_l}^{cc}(\epsilon - \epsilon_F + i\Gamma_h)}{2l + 1} \right] \\ = & \sigma_{\text{at}} + \sigma_{\text{env}}. \end{aligned} \quad (4)$$

Here the term represented by the first two lines of Eq. (4) refers to the atomiclike absorption (of the scatterer placed at site  $c$ )  $\sigma_{\text{at}}$ ; the remaining addend [see the third line of Eq. (4)] refers to the contribution of the environment (given by other scatterers)  $\sigma_{\text{env}}$ .

$G_{l m_l, l m_l}^{cc}$  is the nonrelativistic full Green's propagator which describes (using perturbation theory, convergent in the EXAFS regime) all closed paths starting at the photoabsorber atom with a core hole (placed in position  $c$  at the center of a cluster) and finishing at the same site. This is a particular case of the more general full Green's propagator [with  $L = (l m_l)$ ]

$$\begin{aligned} G_{LL}^{ij}(\epsilon) = & G_{0LL}^{ij}(1 - \delta_{i,j}) \\ & + \sum_{q \neq i,j} \sum_{L'} G_{0LL'}^{iq}(\epsilon) t_{L'}^q(\epsilon) G_{L'L}^{qj}(\epsilon) + \dots \end{aligned} \quad (5)$$

$G_0^{ij}$  describes the free-electron propagation in the interstitial region between muffin-tin potentials placed at sites  $i$  and  $j$  (with  $k = p = \sqrt{\epsilon}$ ) [14]:

$$\begin{aligned} G_{LL}^{ij}(\epsilon) = & -4\pi i \sum_{L''} i^{l-l''-l''} C_{LL''}^{L'} h_{L''}^+(kR_{ij}), \\ C_{LL''}^{L'} = & \int d\hat{r} Y_L(\hat{r}) Y_{L'}(\hat{r}) (Y_{L''}(\hat{r}))^* \end{aligned} \quad (6)$$

and  $t_l^j$  are the components for given angular momentum  $l$  and atom  $j$  of the atomic  $t$  matrix given by smooth matching at the muffin-tin radius  $r_s$  of the regular upper Dirac component inside the muffin-tin sphere with the free solution outside the sphere (notice that the  $t$  matrix is exactly determined by the

knowledge of the upper Dirac component even in the fully relativistic description of [7])

$$t_l(\epsilon) = i \frac{[g_l(r) j_l'(kr) - g_l'(r) j_l(kr)]}{[g_l(r) (h_l^+)'(kr) - g_l'(r) h_l^+(kr)]} \Big|_{r=r_s}. \quad (7)$$

In this work relativistic corrections are tested for atomic phase shifts  $\delta_l$ . These can be obtained from atomic  $t$  matrices by means of the expression

$$t_l^j = e^{i\delta_l^j} \sin(\delta_l^j). \quad (8)$$

Formulas from (4) to (7) are appropriate for the scalar-relativistic description of Eq. (2) [omitting the (so) term].

In routine calculations, Eq. (2) can be numerically solved by the Numerov procedure after elimination of the first-order derivative, by applying the method of Gaussian elimination [17]. The more flexible linear-logarithm mesh [18] should be used instead of the usual Herman-Skillman mesh.

The scalar-relativistic corrections discussed above have been implemented in the GNXAS suite of programs, by modifying only the PHAGEN program which calculates the  $t$  matrices (defining the phase-shift functions) through Eq. (7) and the atomic absorption cross section [see the contribution  $\sigma_{\text{at}}$  to Eq. (4)].

### III. RESULTS OF THE SIMULATIONS

#### A. Phase-shift calculations

The mass and Darwin terms of Eq. (2) are known to yield collectively a potential which is attractive, pulling in

TABLE I. List of 12 representative elemental systems. For each atom type we report the atomic number  $Z$ , the structure (all elements correspond to crystalline solids with the exception of Br, which is a diatomic molecular system in the gas phase);  $a$ ,  $b$ ,  $c$  (real-space lattice parameters);  $R_1$  (nearest-neighbor separation);  $r_{\text{MT}}$  (muffin-tin radius for the photoabsorbing atom);  $\Gamma_h$  (HWHM core hole width for the absorption edges shown in brackets [31]).

Cluster	$Z$	Structure	$a$ (Å)	$b$ (Å)	$c$ (Å)	$R_1$ (Å)	$r_{\text{MT}}$ (Å)	$\Gamma_h$ (eV)
Ne	10	fcc [19]	3.7860			2.677	1.018	0.12 ( $K$ )
Si	14	diam. c [20]	5.4309			2.352	1.120	0.24 ( $K$ )
Ca	20	fcc [21]	5.56			3.932	1.569	0.41 ( $K$ ), 0.09 ( $L_3$ )
Zn	30	hcp [22]	2.6648		4.9467	2.665	1.099	0.84 ( $K$ ), 0.33 ( $L_3$ )
Br	35	diat. mol [23]				2.286	1.085	1.26 ( $K$ ), 0.54 ( $L_3$ )
Zr	40	hcp [24]	3.232		5.147	3.179	1.282	1.92 ( $K$ ), 0.79 ( $L_3$ )
In	49	bct [25]	3.2523		4.9461	3.252	1.322	3.96 ( $K$ ), 1.33 ( $L_3$ )
Nd	60	hcp [26]	3.658		11.799	3.658	1.632	8.65 ( $K$ ), 1.83 ( $L_3$ )
Yb	70	fcc [27]	5.4847			3.879	1.541	15.96 ( $K$ ), 2.30 ( $L_3$ )
Au	79	fcc [28]	4.0782			2.884	1.136	26.01 ( $K$ ), 2.71 ( $L_3$ )
Pb	82	fcc [29]	4.9396			3.493	1.376	30.21 ( $K$ ), 2.91 ( $L_3$ )
Th	90	fcc [30]	5.0843			3.595	1.429	44.02 ( $K$ ), 3.57 ( $L_3$ )

scattered photoelectron waves and increasing the magnitude of the real part of atomic phase shifts [7]. This effect has been investigated for 12 elemental condensed systems, for atomic numbers ranging from 10 (for Ne) to 90 (for Th). Mainly solid crystalline systems (mostly face-centered-cubic, fcc) at room temperature and normal pressure have been considered with two notable exceptions. Face-centered-cubic crystalline Ne is supposed to be at pressure  $P > 4.74$  GPa and at room temperature; diatomic molecular bromine considered in the gas phase at normal pressure and room temperature. The relevant information about the elements under study is summarized in Table I.

For each system the CRYMOL and GNPEAK programs (of the GNXAS package) have been used to define a fixed-atom reference pattern, with particular attention to the structural data reported in the literature, as specified in Table I.

Muffin-tin radii have been generated using the Norman criterion [32], suitably rescaled as it is a standard choice for XAFS calculations. The values  $r_{\text{MT}}$  of these radii for the atoms with a core hole are reported in Table I.

A complex Hedin-Lundqvist optical potential has been chosen in all cases to account for energy-dependent exchange effects and inelastic losses. Calculations have been made over a wide range of wave-vector values above the edge,  $k_{\text{max}} \sim 18 \text{ \AA}^{-1}$ .

Phase-shift calculations have been made for all the elements of Table I, typically up to  $l_{\text{max}} = k_{\text{max}} \times r_{\text{MT}}$  values, and shown here for the lower partial waves  $l = 0, 1, 2, 3$ , as a function of the photoelectron kinetic energy (see Fig. 1). The examples shown in Fig. 1 are related to In ( $L_3$  edge) and Au ( $L_3$  edge) and refer to the photoabsorbing atoms (i.e., with a core hole). No substantial differences have been found considering neutral atoms, either surrounded by neutral atoms or including also a neighboring excited photoabsorber atom.

The real part of the atomic phase shifts  $\delta_l$  ( $l = 0, 1, 2, 3$ ) for In (upper figure) and Au (lower figure) are shown in the left panels of Fig. 1. Nonrelativistic (nr) and scalar-relativistic (sr) corrections are indicated, respectively, by blue and orange (continuous) lines; spin-orbit relativistic (sojp,  $j = l + 1/2$ )

and (sojm,  $j = l - 1/2$ ) are denoted, respectively, by green and red (dashed) lines. The differences between nonrelativistic (nr) and scalar-relativistic (sr) phase shifts ( $|\text{Re}\{\delta_l^{\text{sr}} - \delta_l^{\text{nr}}\}|$ ), averaged over five consecutive energy-mesh points, are shown in the right-hand-side panels of Fig. 1. The overall average energy difference is also represented as a green line.

Differences between scalar-relativistic and nonrelativistic phase shifts have been found to be a smooth function over the entire energy range of interest for XAFS. This deviation reaches 0.5 radians for the  $s$  wave for Au ( $Z = 79$ ), underlying the importance of relativistic effects for this heavy element, with respect to the lighter In ( $Z = 49$ ) (for which the deviation in the  $s$  wave amounts to 0.2). We have also verified that present scalar-relativistic calculations of the phase shifts are in good agreement with those calculated by FEFF [9] using the same atomic coordinates.

The results of relativistic phase-shift calculations are summarized in Fig. 2, where we show the differences between (sr) and (nr) phase shifts for the various systems reported in Table I as a function of the atomic number. The magnitude of the correction is reported in Fig. 2 for the first four partial waves  $l = 0$  (pink line),  $l = 1$  (green line),  $l = 2$  (blue line),  $l = 3$  (brown line), and for both the  $K$  edge (points marked by a star) and the  $L_3$  edge (points marked by a square). The arithmetic average between the  $K$ -edge and the  $L_3$ -edge points is also reported as a dashed curve. The effect of the mass and Darwin terms in pulling upwards the real part of atomic phase shifts with respect to the nonrelativistic case goes roughly as  $(\alpha Z)^2$ , as it is clear looking at the  $s$ - and  $p$ -wave curves as compared with the  $(Z/137)^2$  curve. The importance of relativistic effects rapidly diminishes with increasing  $l$  (and increasing photoelectron wave vector or energy), because of the screening provided by the centrifugal barrier in the region close to the nuclei.

No substantial differences in phase-shift relativistic corrections have been found between the  $K$ -edge and  $L_3$ -edge cases. This is also in line with the fact that the scattering power has been found to be nearly the same, independently of the fact that the atom is neutral or with a core hole.

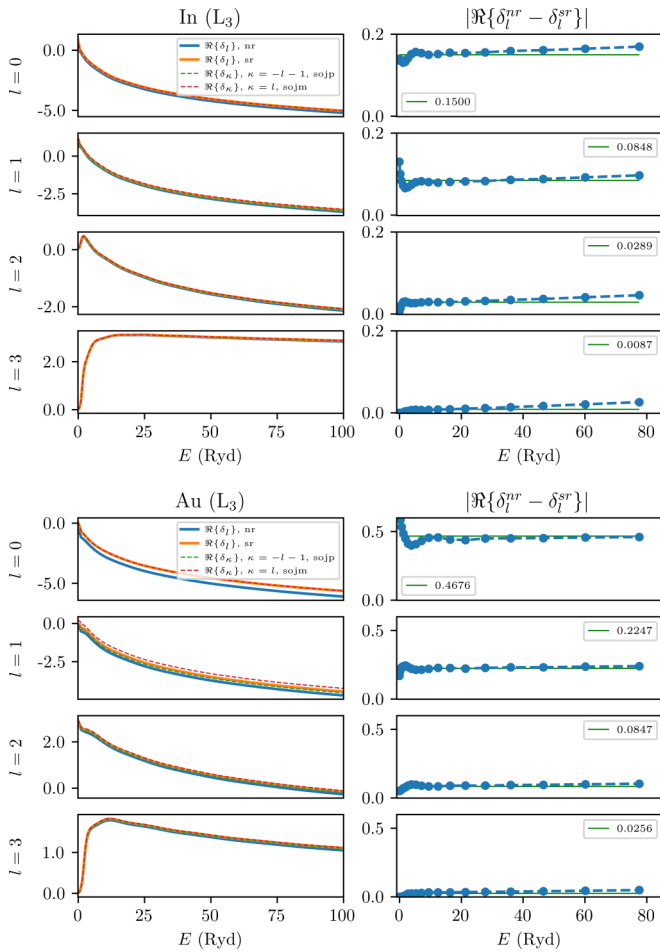


FIG. 1. Left panels: phase shifts  $\delta_l$  ( $l = 0, l = 1, l = 2, l = 3$ ) (real part) for the photoabsorbing In ( $L_3$  edge) atom in a body-centered-tetragonal crystalline system (upper figures) and of Au ( $L_3$  edge) atoms in fcc crystalline gold (lower figures) calculated by the new PHAGEN program as a function of the photoelectron energy. Nonrelativistic (nr) and scalar-relativistic (sr) corrections are indicated, respectively, by blue and orange (continuous) lines; spin-orbit relativistic (sojp,  $j = l + 1/2$ ) and (sojm,  $j = l - 1/2$ ) are denoted, respectively, by green and red (dashed) lines. Right-hand panels: difference between nonrelativistic (nr) and scalar-relativistic (sr) phase-shift calculations for In and Au. The importance of accounting for relativistic effects in Au is evident. All phase shifts and differences are shown in rads.

## B. Calculated XAFS signals

The calculated nonrelativistic and scalar-relativistic atomic phase shifts have been combined with a fixed-atom geometrical arrangement to build up theoretical multiple-scattering XAFS signals, by means of the GNXAS subprogram. Figures 3–5 show the example of the single-scattering (dominant) contribution  $\chi_2$  to the first-neighbor signal  $\gamma_1^{(2)}$  [2], in the case of, respectively, crystalline calcium, neodymium, and gold. The panels report from top to bottom: the total single-scattering signals  $\chi(k) = A(k) \sin[\phi(k)]$ ; amplitudes  $A(k)$ ; and total phase functions  $\Psi(k) = \phi(k) - 2kR_1$  ( $R_1$  being the nearest-neighbor separation specified in Table I). The lower curves display the difference of (nr) and (sr) amplitudes,

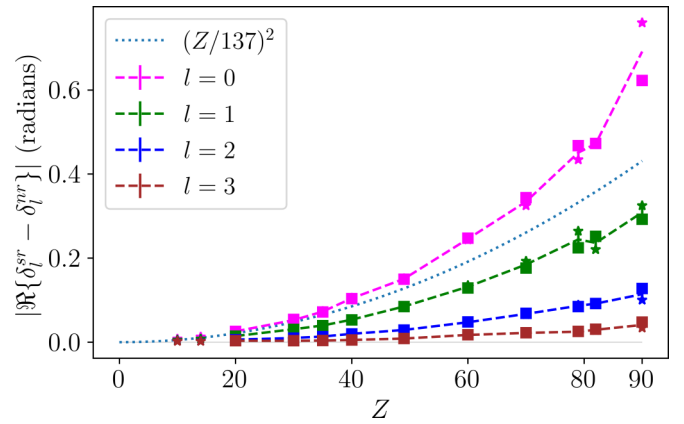


FIG. 2. Differences between scalar-relativistic (sr) and nonrelativistic (nr) phase shifts as a function of the atomic number  $Z$ , calculated by means of the new PHAGEN program; for the partial waves  $l = 0$  (pink color),  $l = 1$  (green color),  $l = 2$  (blue color),  $l = 3$  (brown color); and for both the  $K$  edge (points marked by a star) and the  $L_3$  edge (points marked by a square). The importance of accounting for relativistic effects in high- $Z$  elements is evident. All phase shifts and differences are shown in rads.

shown via normalized residuals  $|\frac{A^{(sr)} - A^{(nr)}}{A^{(nr)}}|$ . This quantity has been averaged over five consecutive points to avoid singular points associated with nearly vanishing amplitudes.

In Figs. 3–5, nonrelativistic (nr) and scalar-relativistic (sr) corrections are indicated, respectively, by blue and orange

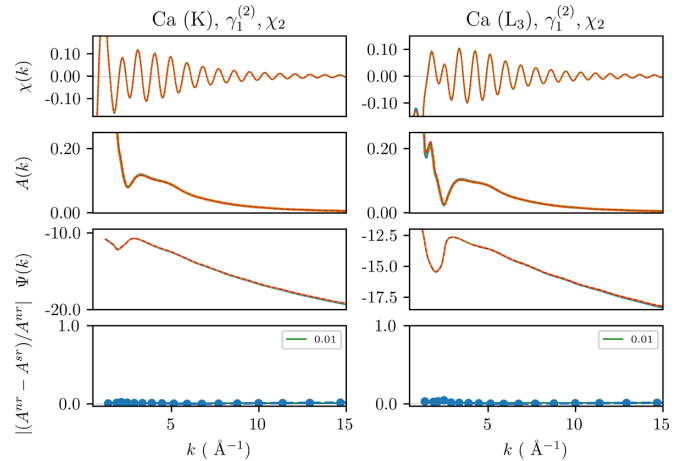


FIG. 3. Results of calculations of the XAFS single-scattering  $\chi_2(k)$  signals (first shell) for solid Ca ( $K$  edge: left panels,  $L_3$  edge: right-hand panels), using structural parameters reported in Table I. From top to bottom, the total single-scattering signals  $\chi(k) = A(k) \sin[\phi(k)]$ , amplitudes  $A(k)$ , and total phase functions  $\Psi(k) = \phi(k) - 2kR_1$  are reported. The panels at the bottom display the difference of (nr) and (sr) amplitudes, reported as normalized residuals  $|\frac{A^{(sr)} - A^{(nr)}}{A^{(nr)}}|$  (averaged over five consecutive energy-mesh points). Nonrelativistic (nr) and scalar-relativistic (sr) corrections are indicated, respectively, by blue and orange (continuous) lines; spin-orbit relativistic (sojp and sojm) are denoted, respectively, by green and red (dashed) lines. The calculated average deviation in  $|\frac{A^{(sr)} - A^{(nr)}}{A^{(nr)}}|$  (over the entire energy range) is also displayed in the lower panels.

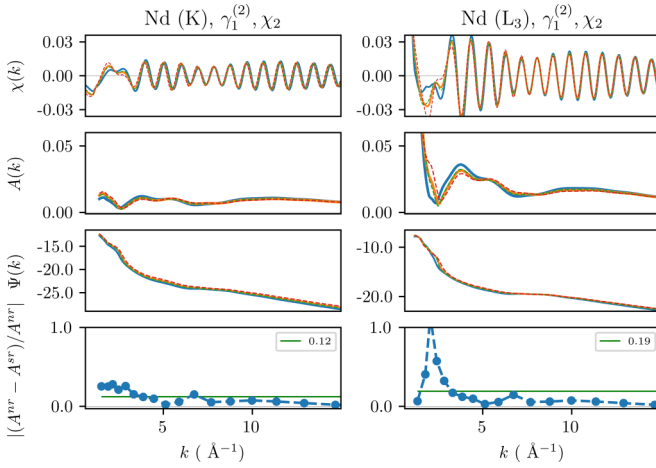


FIG. 4. XAFS calculations for solid Nd ( $K$  edge, left panels;  $L_3$  edge, right-hand panels). The same definitions as in Fig. 3 have been used.

(continuous) lines; spin-orbit relativistic (sojp and sojm) are denoted, respectively, by green and red (dashed) lines. The calculated average deviation in  $|\frac{A^{(sr)} - A^{(nr)}}{A^{(nr)}}|$  (over the entire wave-vector range of interest for XAFS) is also displayed in the lower panels. These values are also reported in the last column of Table II.

Figure 3 displays the  $\chi_2$  signals for solid Ca, comparing the  $K$ -edge (left panels) with the  $L_3$ -edge (right panels) results. No substantial differences between nonrelativistic and relativistic curves have been observed for Ca ( $K$  edge), Ca ( $L_3$  edge), as indicated by the average normalized residuals amounting to  $\sim 1\%$  in both cases. The total phase function  $\Psi(k)$  has a general smoothly decreasing trend as a function of the photoelectron wave vector  $k$ . This trend is subject, however, to sudden changes by  $\sim \pm\pi$  in correspondence of minima or  $A(k)$  (especially those which reach values close to zero), a feature also noted previously [7]. In Fig. 3 this is especially evident for Ca ( $L_3$ ) at  $k \sim 3 \text{ \AA}^{-1}$ .

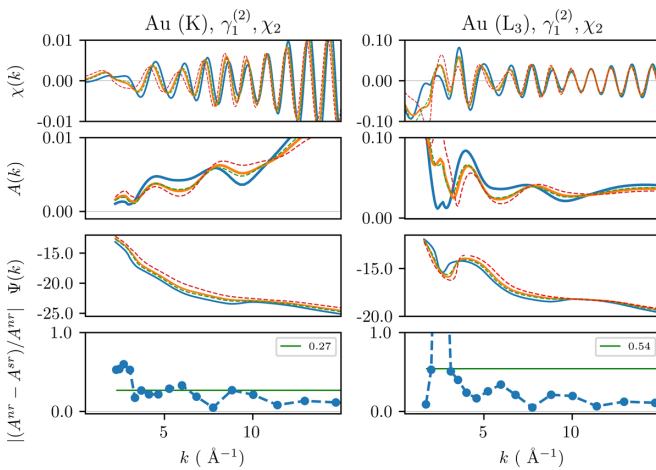


FIG. 5. XAFS calculations for solid Au ( $K$  edge, left panels;  $L_3$  edge, right-hand panels). The same definitions as in Fig. 3 have been used.

TABLE II. Results of the quantitative comparison of scalar-relativistic (sr) and nonrelativistic (nr) calculations made by the new PHAGEN program for the elements of Table I. Average differences (over the entire energy range) between (sr) and (nr) phase shifts (real parts) are reported for  $l = 0, 1, 2, 3$  in the central columns (all differences of phase shifts are expressed in rads). The last column on the right-hand side collects the average (over the entire energy range) relative difference between (nr) and (sr) amplitudes of calculated  $\gamma_1^{(2)}$  (single-scattering) signals (all normalized differences are expressed as percentage).

Cluster (edge)	$\text{Re}\{\delta_l^{\text{sr}} - \delta_l^{\text{nr}}\}$				$ \frac{A^{\text{nr}} - A^{\text{sr}}}{A^{\text{nr}}} $ (%)
	$l = 0$	$l = 1$	$l = 2$	$l = 3$	
Ne ( $K$ )	0.0078	0.0050	0.0028	0.0023	0
Si ( $K$ )	0.0124	0.0075	0.0033	0.0024	0
Ca ( $K$ )	0.0261	0.0149	0.0062	0.0035	1
Ca ( $L_3$ )	0.0255	0.0143	0.0060	0.0036	1
Zn ( $K$ )	0.0511	0.0314	0.0101	0.0034	3
Zn ( $L_3$ )	0.0541	0.0304	0.0098	0.0034	3
Br ( $K$ )	0.0736	0.0401	0.0136	0.0040	5
Br ( $L_3$ )	0.0720	0.0393	0.0134	0.0039	6
Zr ( $K$ )	0.1051	0.0543	0.0200	0.0053	4
Zr ( $L_3$ )	0.1036	0.0529	0.0198	0.0053	10
In ( $K$ )	0.1514	0.0851	0.0293	0.0086	5
In ( $L_3$ )	0.1500	0.0848	0.0289	0.0087	6
Nd ( $K$ )	0.2440	0.1350	0.0468	0.0169	12
Nd ( $L_3$ )	0.2475	0.1288	0.0481	0.0176	19
Yb ( $K$ )	0.3249	0.1930	0.0660	0.0216	15
Yb ( $L_3$ )	0.3438	0.1764	0.0686	0.0226	22
Au ( $K$ )	0.4343	0.2645	0.0885	0.0243	27
Au ( $L_3$ )	0.4676	0.2247	0.0847	0.0256	54
Pb ( $K$ )	0.4715	0.2205	0.0915	0.0281	20
Pb ( $L_3$ )	0.4730	0.2519	0.0921	0.0309	22
Th ( $K$ )	0.7603	0.3251	0.1003	0.0342	19
Th ( $L_3$ )	0.6227	0.2925	0.1279	0.0479	15

Figure 4 displays calculated  $\chi_2(k)$  signals for solid Nd.  $K$ -edge (left panels) and  $L_3$ -edge (right panels) signals are similar in shape for  $k > 4 \text{ \AA}^{-1}$ , but the former is a factor of  $\sim 2$  lower in magnitude (being stronger damped by the core-hole width:  $\Gamma_h = 8.65 \text{ eV}$  for the  $K$  edge,  $\Gamma_h = 1.83 \text{ eV}$  for the  $L_3$  edge)). Large differences between the  $K$ -edge and the  $L_3$ -edge  $\chi_2(k)$  signals can be observed for  $k \lesssim 3 \text{ \AA}^{-1}$ . This region is also characterized by substantial modifications between nonrelativistic and relativistic curves: around  $k \sim 3 \text{ \AA}^{-1}$  and  $k \sim 6 \text{ \AA}^{-1}$ , where both  $K$  and  $L_3$  amplitudes show a minimum, typical beats in the XAFS  $\chi(k)$  signals can be seen. Deviations between (nr) and (sr) amplitudes amount to less than 10% in the typical XAFS range  $k > 4 \text{ \AA}^{-1}$  for both the  $K$  and  $L_3$  edges. The situation is different for  $k < 4 \text{ \AA}^{-1}$  where the normalized residuals show a pronounced peak for the  $L_3$  edge, and a smoother increase for the  $K$  edge (leading to an average deviation of, respectively, 19% and 12%).

Figure 5 shows the interesting case of gold. The Au  $K$ -edge  $\chi_2(k)$  signal (left-hand-side panels) is much more damped with respect to the  $L_3$  signal (right-hand-side panels) because of the much larger core-hole width, 26.01 eV ( $K$  edge) against 2.71 eV ( $L_3$  edge). The importance of accounting for relativistic effects in Au is evident in the whole XAFS range.

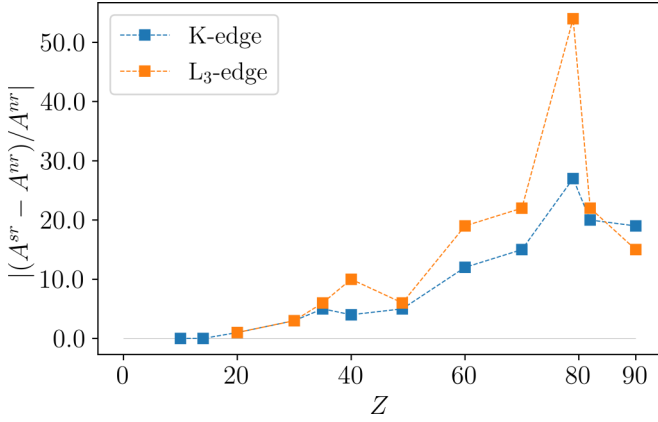


FIG. 6. Normalized difference of nonrelativistic and scalar-relativistic amplitudes (averaged over the entire energy range and expressed as percentage) calculated by new PHAGEN and GNXAS programs, as a function of the atomic number. Only elements of Table I have been considered. Values for the  $K$  and  $L_3$  edges are denoted, respectively, by blue and orange squares. All normalized differences are expressed as percentage.

Relativistic deviations amount to  $\sim 20\%$  for  $k > 5 \text{ \AA}^{-1}$  for both  $K$  and  $L_3$  edges. But for  $k < 5 \text{ \AA}^{-1}$  a large peak in the residuals  $|\frac{A^{(sr)} - A^{(nr)}}{A^{(nr)}}|$  occurs for the  $L_3$  edge in correspondence of beats of (nr) and (sr)  $\chi_2(k)$  signals (at  $k \sim 3 \text{ \AA}^{-1}$ ). A peak in the normalized residuals can be seen also for the  $K$  edge around  $k \sim 3 \text{ \AA}^{-1}$ , but much less pronounced with respect to the  $L_3$  edge. The overall amount of relativistic effects, evaluated by the average normalized residuals, is 54% ( $L_3$  edge) and 27% ( $K$  edge) for solid Au.

Figure 6 reports difference of nonrelativistic and scalar-relativistic XAFS  $\chi_2(k)$  amplitudes (averaged over the energy range of interest for XAFS) as a function of the atomic number, for all elements of Table I. Here blue and orange colors refers to  $K$ -edge and  $L_3$ -edge calculations, respectively.

While relativistic effects have been found to increase phase shifts roughly as  $(Z\alpha)^2$  (see Fig. 2, dotted and  $l = 0$  points), no analogous regular trend can be seen for the average amplitudes of XAFS signals reported in Fig. 6. Indeed, the size of relativistic effects in XAFS signals depends not only on the atomic number and scattering power of the atoms, but also on their geometrical arrangement and on the core-hole lifetime (which contributes to the damping of the amplitude).

In any case, relativistic deviations in amplitudes have been found to exceed 10% for  $Z \gtrsim 60$ . Also in Fig. 6 one can observe a clear peak of relativistic effects in the case of Au ( $Z = 79$ ), which is more pronounced with respect to the heavier Pb ( $Z = 82$ ) and Th ( $Z = 90$ ). This is in line with the literature [33,34], where gold is known to present particularly strong relativistic effects in its chemical and physical properties, and appears to be related to the shorter interatomic distances observed in crystalline Au as compared to Pb and Th.

A summary of the results of the present calculations of relativistic corrections for phase shifts and amplitudes is presented in Table II. The importance of taking account of relativistic corrections for large- $Z$  atoms is clearly assessed by the size of the average deviations in amplitudes observed

TABLE III. Averaged relativistic corrections obtained in two typical fcc crystalline systems (Au and Pb) for the two-body and three-body XAFS ( $\gamma_m^{(n)}$ ) contributions related to first-neighbor distances  $R_1$ . The first-shell distance was fixed to 2.884 and 3.493  $\text{\AA}$  for Au and Pb, respectively. The columns indicate, from the first to the last, the type of the structural configuration, shell number or angle for the triangular arrangement, effective distance for the XAFS signal (semi-perimeter of the two-leg or three-leg configuration), type of XAFS signal, and average (over the entire energy range) of the normalized residuals  $|\frac{A^{(sr)} - A^{(nr)}}{A^{(nr)}}|$  of the amplitudes of the XAFS signals calculated using the GNXAS and the new PHAGEN program, for Au ( $L_3$  edge) and Pb ( $L_3$  edge). Those values are expressed in percentages.

Struct. config.	Shell no. (angle)	Effective distance	MS signal	$ \frac{A^{(nr)} - A^{(sr)}}{A^{(nr)}} $ (%)	
				Au ( $L_3$ )	Pb ( $L_3$ )
Two-body	1	$R_1$	$\gamma_1^{(2)}$	54	22
Three-body	$60^\circ$	$\frac{3}{2}R_1$	$\gamma_1^{(3)}$	34	31
Two-body	2	$R_2 = \sqrt{2}R_1$	$\gamma_2^{(2)}$	25	17
Three-body	$90^\circ$	$\frac{2+\sqrt{2}}{2}R_1$	$\gamma_2^{(3)}$	26	34
Two-body	3	$R_3 = \sqrt{3}R_1$	$\gamma_3^{(2)}$	18	16
Three-body	$120^\circ$	$\frac{2+\sqrt{3}}{2}R_1$	$\gamma_3^{(3)}$	23	28
Two-body	4	$R_4 = 2R_1$	$\gamma_4^{(2)}$	17	16
Three-body	$180^\circ$	$2R_1$	$\gamma_4^{(3)}$	39	32

in the entire XAFS range reported in the last column. On the other hand, the large deviations observed for the phase shifts with low angular momenta suggest that relativistic calculations must be used for near-edge XAS calculations.

The effect of relativistic corrections has been also studied for  $n$ -body XAS signals related to atoms beyond the first-neighbor coordination shells. We have thus calculated higher-order MS XAFS signals related to the  $n$  body  $\gamma_2^{(2)}$ ,  $\gamma_3^{(2)}$ ,  $\gamma_1^{(3)}$ ,  $\gamma_2^{(3)}$ ,  $\gamma_3^{(3)}$ ,  $\gamma_4^{(3)}$  [3] contributions up to the fourth coordination shell, in the case of fcc crystalline gold (Au,  $L_3$  edge) and lead (Pb,  $L_3$  edge). The  $\gamma_2^{(2)}$ ,  $\gamma_3^{(2)}$ ,  $\gamma_4^{(2)}$  signals are two-body contributions of the second, third, and fourth shells. The  $\gamma_1^{(3)}$ ,  $\gamma_2^{(3)}$ ,  $\gamma_3^{(3)}$ , and  $\gamma_4^{(3)}$  contributions denote, for a fcc crystalline system, three-body configurations with first neighbors at given bond angles, respectively,  $60^\circ$ ,  $90^\circ$ ,  $120^\circ$ , and  $180^\circ$ . Calculations follow the scheme reported in Ref. [3] for fcc crystals and relevant data are reported in Table III.

As an example, we show in Fig. 7 the results for the  $\gamma_4^{(3)}$  contribution (the so-called linear-focusing one), calculated by means of the new PHAGEN and GNXAS programs, for Au ( $L_3$ ) and Pb ( $L_3$ ). The curves presented in Fig. 7 are defined as in Figs. 3–5, but in this case the effective distance  $R$  used to calculate  $\Psi(k) = \phi(k) - 2kR$  is the semiperimeter of the shorter MS path ( $2R_1$  for  $180^\circ$  configurations). The difference between calculations performed using scalar-relativistic and nonrelativistic phase shifts is evident in the whole energy ( $k$ ) range.

The results for the average deviation of the amplitudes  $|\frac{A^{(sr)} - A^{(nr)}}{A^{(nr)}}|$  in  $\gamma_2^{(2)}$ ,  $\gamma_3^{(2)}$ ,  $\gamma_1^{(3)}$ ,  $\gamma_2^{(3)}$ ,  $\gamma_3^{(3)}$ ,  $\gamma_4^{(3)}$  signals are presented in Table III. From Table III it is clear that relativistic effects, in the two-body contributions  $\gamma^{(2)}$ , decrease as the shell distance increases. Relativistic effects in the three-body

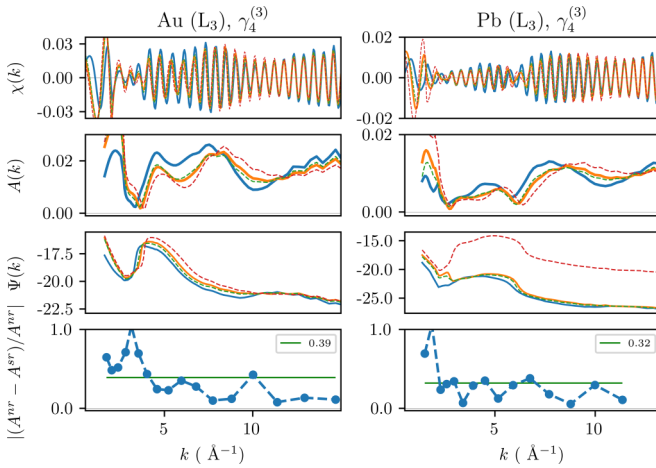


FIG. 7. Total calculated  $\gamma_4^{(3)}$  signal (first-neighbor three-body contribution at angle  $180^\circ$ ) as a function of the photoelectron wave vector  $k$ , for Au ( $L_3$  edge) (left panels) and Pb ( $L_3$  edge) (right panels). From top to bottom, the total XAFS signals, amplitudes  $A(k)$ , and total phase functions  $\Psi(k) = \phi(k) - 2kR$  (see Table III for the definition of the effective distance  $R$ ) are reported. The panels at the bottom display the difference of (nr) and (sr) amplitudes, reported as normalized residuals  $|A^{(sr)} - A^{(nr)}| / A^{(nr)}$  (averaged over five consecutive energy-mesh points). Nonrelativistic (nr) and scalar-relativistic (sr) corrections are indicated, respectively, by blue and orange (continuous) lines; spin-orbit relativistic (sojp and sojm) are denoted, respectively, by green and red (dashed) lines. The calculated average deviation in  $|A^{(sr)} - A^{(nr)}| / A^{(nr)}$  (over the entire energy range) is also displayed in the lower panels.

contributions  $\gamma_1^{(3)}$ ,  $\gamma_2^{(3)}$ ,  $\gamma_3^{(3)}$ ,  $\gamma_4^{(3)}$  have been found to be larger than the corresponding two-body signals  $\gamma_2^{(2)}$  (second shell),  $\gamma_3^{(2)}$  (third shell), even though the overall path effective distances are larger for three-body MS contributions. A possible explanation of this effect is that typically three-body signals involve the product of one more  $t$  matrix effected by relativistic corrections [7]. Relativistic corrections in the linear focusing  $\gamma_4^{(3)}$  signal have been found to be particularly strong (even though the path effective distance is the longest). Finally, comparing Au ( $L_3$  edge) and Pb ( $L_3$  edge) cases, relativistic corrections in the two-body  $\gamma^{(2)}$  and in the linear-focusing term  $\gamma_4^{(3)}$  have been found to be more pronounced in the former case, while relativistic deviations in the remaining  $\gamma_1^{(3)}$ ,  $\gamma_2^{(3)}$ ,  $\gamma_3^{(3)}$  signals are very similar in both cases.

### C. Application to crystalline gold

As discussed in the preceding sections,  $L_3$  XAFS spectra of solid Au are expected to contain important relativistic corrections. As shown in Figs. 5 and 7 and Table II variations up to 50% can be observed as compared to nonrelativistic calculations. We have performed a full structural refinement of the Au  $L_3$ -edge experimental signal of face-centered-cubic (fcc) crystalline Au measured at room temperature (foil of nominal thickness  $4 \mu\text{m}$ ). XAFS data were originally collected using synchrotron radiation at the LURE (Orsay, France) beamline D42-EXAFS 1 (bending magnet source) equipped

with a channel-cut Si(331) monochromator (bending magnet source). Estimated noise-to-signal ratio of the raw XAFS data was  $2 \times 10^{-4}$ .

XAFS refinements were carried out using both scalar-relativistic (sr) and nonrelativistic (nr) approximations, within the GNXAS data-analysis method discussed above. The individual irreducible multiple-scattering signals related to a typical fcc structure [2,3] were calculated up to the fourth coordination shell as reported in Table III.

An important aspect of the XAFS data analysis is the modeling of the atomic background that for the Au  $L_3$  edge is particularly complex, being affected by the presence of multielectron channels involving mainly the excitation of  $4f$  electrons as discussed in previous papers [35,36]. The absorption background used in the present structural refinement includes a smooth polynomial spline and the contribution of double-electron excitation  $2p4f$  and  $2p4d$  channels, respectively, around 110 and 350 eV above the  $L_3$  edge.

The results of the XAFS structural refinements are reported in Fig. 8, where scalar-relativistic and nonrelativistic best-fit calculated signals are compared with the experimental  $L_3$  XAFS of crystalline Au measured at 300 K. The individual MS signals related to the first four coordination shells are also reported in Fig. 8, including the dominant  $\gamma_1^{(2)}$  first-shell contribution; the pure three-body  $\gamma_1^{(3)}$  term associated with first-neighbor equilateral configurations; the  $\eta_2^{(3)}$ ,  $\eta_3^{(3)}$ , and  $\eta_4^{(3)}$  terms associated with second, third, and fourth shell atoms, respectively. The  $\eta^{(3)}$  signals include both two-body and three-body contributions due to  $90^\circ$ ,  $120^\circ$ , and  $180^\circ$  first-neighbor configurations.

As shown in Fig. 8, a clear improvement in the agreement is obtained using scalar-relativistic (sr) phase shifts. This is shown by the marked decrease in the residual value (around 2.6 for sr calculations) and can be also appreciated looking at the Fourier transform (FT) of both calculations reported in the right-hand panel of Fig. 8. A significant increase in the agreement between experimental and calculated MS signals is obtained using (sr) calculations, especially in the  $4\text{--}12 \text{ \AA}^{-1}$  wave-vector range. The FT of the nonrelativistic (nr) best-fit signal does not accurately reproduce the first-shell contribution (double-peak structure in the  $2\text{--}3 \text{ \AA}$  region) as it can be seen looking both at the FT of the nr XAFS best-fit calculations and at the FT of the difference with the experimental spectrum (respectively nr calc. blue dotted line in Fig. 8). On the other hand, the FTs of experimental and calculated sr signals are in good agreement and the residual curve shows mainly random fluctuations.

Of course, it is also important to verify that the results XAFS structural refinements are consistent with literature data. The most important structural parameters are those related to the first-neighbor distribution, namely, the average nearest interatomic distance  $R$ , the mean-square relative displacement  $\sigma^2$  (bond variance appearing in the Debye-Waller-type factor), and the skewness  $\beta$  (related directly to the third cumulant of the distribution  $\beta = C_3/\sigma^3$ ). The last parameter is different from zero for distributions departing from a simple Gaussian for increasing lattice temperatures. Even for moderate temperatures, departures from a simple Gaussian behavior is observed in most metals, and this is

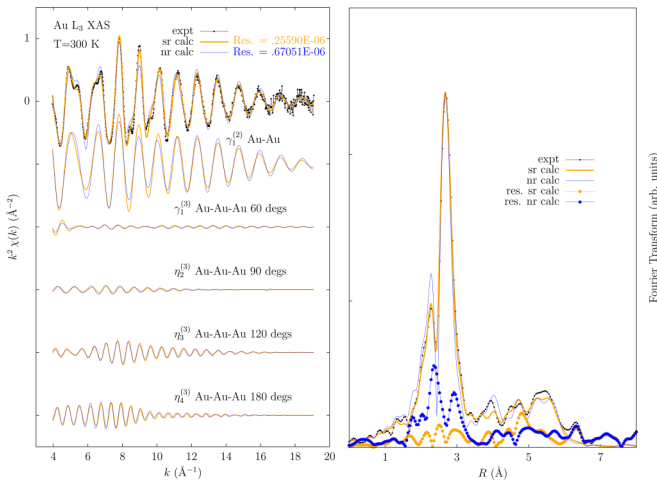


FIG. 8. XAS Au  $L_3$ -edge structural refinement (face-centered-cubic crystal, 299 K) using the GNXAS data-analysis method using scalar-relativistic (sr, orange) and nonrelativistic (nr, blue) approximations. Left panel: comparison between the experimental (expt., black dotted line) and best-fit multiple-scattering total calculated signals using sr (orange) and nr (blue) approximations (upper curves). The total signals include contributions up to the fourth shell. From top to the bottom the individual irreducible multiple-scattering signals up to the fourth coordination shell are reported (first neighbors  $\gamma_1^{(2)}$ , equilateral configurations  $\gamma_1^{(3)}$ , second  $\eta_2^{(3)}$ , third  $\eta_3^{(3)}$ , and fourth  $\eta_4^{(3)}$  shells corresponding to first-neighbor configurations at  $90^\circ$ ,  $120^\circ$ , and  $180^\circ$ ). The improvement in XAFS refinement obtained using sr calculations is evident and can be appreciated looking at the decrease in the residual function ( $\sim 2.6$ ). Visible differences in the simulations can be observed especially in the  $5\text{--}10 \text{ \AA}^{-1}$  range. Right-hand panel: Fourier transform of the total signals reported in the left panel ( $k$  range:  $4\text{--}19 \text{ \AA}^{-1}$ ). The improvement in the agreement obtained using relativistic calculations is evident. The characteristic double peak in the  $2\text{--}3 \text{ \AA}$  region, related to the first neighbors, is correctly reproduced only by relativistic calculations (sr, orange). The Fourier transforms of the residual spectra (difference between experimental and calculated signals) show clearly deviations beyond the noise level.

the case also of crystalline Au [37]. Coordination numbers and average angles for the first four shells and three-body configurations have been kept fixed to those of a standard fcc lattice [3].

The best-fit parameters of the present XAFS refinements are reported in the first two columns of Table IV (sr, nr), and compared with results reported in the literature [37,38]. The first-neighbor average distance  $R$ , reported in the first row of Table IV, is usually measured by XAFS with high precision (typically  $0.005 \text{ \AA}$ ) and should be compared with the interatomic distance resulting from the lattice parameter  $R_0 = a/\sqrt{2} = 2.884 \text{ \AA}$  measured by diffraction [39]. The values reported in the first row are all compatible with the lattice distance  $R_0$  measured at 300 K with the possible exception of that obtained by nonrelativistic phase shifts. In fact, the average interatomic distance measured by XAFS can be approximated at the lowest order  $R \sim R_0 + \sigma_\perp^2/R_0$  (see [40] and references therein) where  $\sigma_\perp^2$  is the vibrational bond variance projected on the plane orthogonal to the average bond direction. In this way,  $R$  must be always slightly larger than

TABLE IV. Best-fit parameters obtained by present XAFS refinements of solid Au at 300 K, compared with results reported in the literature. Relevant XAFS parameters related to the first-neighbor Au-Au distribution ( $R$ ,  $\sigma^2$ , and  $\beta$ ) are listed in the first column and discussed in the text, as well as the nonstructural parameters  $E_0$  and  $S_0^2$ . The last row contains the final value of the residual function indicating the agreement with the experimental data. From left to right the columns report the results for the present XAFS refinements (sr and nr); those of a previous XAFS work [38]; range of first-neighbor structural parameters obtained by molecular-dynamics simulations (MD) using different interatomic potentials [37]; estimate of the first-shell bond variance  $\sigma^2$  obtained by an Einstein vibrational model [41] using a suitable range of Debye temperatures valid for Au [39] (ED model).

Au (300 K)	XAFS (sr)	XAFS (nr)	XAFS [38]	MD [37]	ED [41] model
$R$ ( $\text{\AA}$ )	2.886	2.899	2.885	2.889–2.904	
$\sigma^2$ ( $10^{-3} \times \text{\AA}^2$ )	8.70	8.84	8.34	9.5–13.5	7.57–9.79
$\beta$	0.35	0.49		0.05–0.4	
$E_0$ (eV)	+7.79	+5.80	+7.3		
$S_0^2$	0.85	0.75	0.9		
Residual ( $10^{-6}$ )	0.256	0.671			

$R_0$  as it is in Table IV. Another interesting parameter is the bond variance  $\sigma^2$  reported in the second row of the same table. Present XAFS results match quite well previous XAFS and molecular-dynamics (MD) results [37,38]. Moreover, the bond variance can be estimated using an Einstein model for vibrations [41] which takes into account the Debye temperature of Au, for which accepted values are presently in the  $T_D = 165\text{--}188 \text{ K}$  range [39]. The value reported in the last column of Table IV reflects this range and is in agreement with present XAFS results. On the other hand, the bond variance calculated by MD using different interatomic force models slightly overestimates the XAFS results. The skewness parameter  $\beta$  measured by XAFS (sr) is in good agreement with previous MD results, as shown in the third row of Table IV. The other typical XAFS nonstructural parameters like  $E_0$  (difference between the experimental and theoretical energy scales) and  $S_0^2$  (amplitude reduction factor for calculations) are reported in the successive rows of Table IV. The  $E_0$  values reported in Table IV refer to the edge energy  $E_e$  of the first inflection point of the Au  $L_3$  edge spectrum ( $E_e = 11\,912.6 \text{ eV}$  for our data). We see that significant deviations are observed for nonrelativistic (nr) best-fit refinements.

The residual values [3] of the XAFS refinement procedures are reported in the bottom row of Table IV, to be compared with the estimated expected value of the residual for the present data set ( $0.229 \times 10^{-6}$ ). The application of scalar-relativistic calculations (sr) clearly improves the quality of the refinement, as shown by a decrease of a factor  $\sim 2.6$  of the residual.

The present XAFS refinements show clearly that scalar-relativistic (sr) calculations improve both the agreement with the experimental data and the accuracy in structural results.

#### IV. CONCLUSIONS

In this work, we have described the inclusion of relativistic corrections in multiple-scattering calculations used for XAFS data analysis of nonmagnetic materials within the GNXAS suite of programs. The validity and accuracy of these calculations have been preliminarily put to a test in a recent work [10] where we have shown a significant improvement in the structural refinement of the XAFS experimental signal of crystalline lead (Pb,  $L_3$  edge) with respect to the nonrelativistic scheme.

Here, this scheme for phase-shift calculations has been put to a test in a wide range, as the atomic number  $Z$  varies between 10 and 90, of known pure-element condensed-state systems. Particular attention has been paid to the comparison of relativistic effects for the  $K$  and the  $L_3$  absorption edges. Nonrelativistic, scalar-relativistic, and fully relativistic scattering  $t$  matrices (and phase shifts) have been calculated for every system under study. Phase-shift corrections have been found to be a smooth, nearly constant function of the photoelectron wave vector; and to be more important for low angular momenta (especially for the  $l = 0$  partial wave, even though in this case the spin-orbit splitting is absent). Therefore, relativistic corrections are particularly important for low photoelectron energies where a small number of low- $l$  partial waves are needed to describe the final state. This conclusion is in line with the following:

(i) the larger size of relativistic effects in the low-wave-vector region (near-edge and nearby structures) of calculated XAFS signals;

(ii) the observed improvement in the agreement of scalar-relativistic calculation with experimental data for fcc crystalline lead (Pb  $L_3$  edge) (with respect to the use of a nonrelativistic fitting scheme), especially for  $k < 6 \text{ \AA}^{-1}$ , as shown in Ref. [10].

Relativistic effects, estimated by the average difference of nonrelativistic and scalar-relativistic phase shifts (real parts), have been found to increase gradually with the atomic number  $Z$ , roughly as a power law  $(\frac{Z}{137})^2$  for  $l = 0$ , and much slower for higher- $l$  partial waves. Relativistic corrections in atomic phase-shift calculations have been found to be weakly affected by the change of the absorption edge (comparing  $K$ - and  $L_3$ -edge signals).

Multiple-scattering calculations of the XAFS structural two-body ( $\gamma^{(2)}$ ) contributions have been carried out systematically showing that amplitude minima are often associated with beats in relativistic and nonrelativistic structure signals, for which relativistic effects reach maximal levels.

Relativistic effects have been found to be particularly important for  $Z \gtrsim 60$ , when amplitude deviations exceed the value of 10% (and phase-shift deviations reach the value of 0.2 rads for the  $s$  wave). A slight predominance of relativistic effects has been found for  $L_3$ -edge amplitudes with respect to  $K$ -edge amplitudes. This difference is found to increase slightly as the atomic number increases, excluding some notable exceptions (In, Pb, Zn, see Fig. 6).

As also discussed previously [33,34], gold has been found to be an element for which relativistic corrections are particularly important. The quality of the structural refinements has been put to a test in the case of crystalline Au at ambient

temperature, showing that relativistic calculations clearly improve the agreement with measured experimental XAFS data providing accurate structural results.

We can summarize our observations as follows:

(i) The monotonic  $Z$  trend of relativistic corrections in atomic phase shifts has shown a (shallow, but noticeable) local maximum of relativistic effects in the case of Au ( $Z = 79$ ) (see Fig. 2).

(ii) The  $Z$  trend of relativistic corrections in the first-shell two-body (calculated) structure signal has presented a clear peak in the case of Au, much higher with respect to the heavier Pb and Th (see Fig. 6). The same maximum of relativistic effects has been found to persist in higher-order XAFS signals, especially for the linear-focusing three-body contribution. This can be easily appreciated comparing Au ( $L_3$ ) and Pb ( $L_3$ ) cases (see Table III) and is largely associated with the higher Au atomic density (shorter interatomic distances).

In view of these results, we can conclude that the scheme implemented in GNXAS for relativistic MS calculations can be safely used for XAFS structural refinements of systems containing atoms for which relativistic corrections are important. In particular, the use of relativistic calculations appears to be necessary typically for large atomic numbers  $Z \gtrsim 60$ , but substantial improvements may be obtained also in an intermediate range  $Z \gtrsim 30$ , both for  $K$  and  $L$  edges.

#### ACKNOWLEDGMENTS

We sincerely thank N. Hara and A. Filipponi for useful discussions about this manuscript. The Au  $L_3$  XAFS data were originally collected during dedicated beamtime at L.U.R.E. DCI synchrotron by A.D.C. and A. Filipponi.

#### APPENDIX

An electron with total energy  $E$  in a central-field potential  $V(r)$  is described by the Dirac equation [42]

$$\begin{aligned} [\boldsymbol{\sigma} \cdot \mathbf{p}] \psi_B &= \frac{1}{c} [E - V(r) - mc^2] \psi_A, \\ [\boldsymbol{\sigma} \cdot \mathbf{p}] \psi_A &= \frac{1}{c} [E - V(r) + mc^2] \psi_B, \end{aligned} \quad (\text{A1})$$

where  $\boldsymbol{\sigma} = (\sigma_x, \sigma_y, \sigma_z)$  is the electron spin in terms of Pauli matrices;  $\mathbf{p} = -i\hbar\nabla$  is the electron relativistic three-momentum.  $\psi_A$  and  $\psi_B$  are, respectively, the upper and lower Dirac components, and a solution to equation (A1) can be found of the form [15]

$$\psi = \begin{pmatrix} \psi_A \\ \psi_B \end{pmatrix} = \begin{pmatrix} g(r) \chi_\kappa^\mu(\hat{r}) \\ if(r) \chi_{-\kappa}^\mu(\hat{r}) \end{pmatrix}. \quad (\text{A2})$$

Here,  $\chi_\kappa^\mu(\hat{r}) \equiv \sum_{\nu=\pm 1} (l_\kappa, \mu - \nu, 1/2, \nu/2 | j_\kappa, \mu) Y_{l_\kappa, \mu - \nu}(\hat{r}) \chi_\nu$  are spin-spherical harmonics, i.e., space-independent eigenstates of the operators  $j^2$ ,  $j_z$ ,  $l^2$ ,  $(\boldsymbol{\sigma} \cdot \mathbf{l} + \hbar)$  with eigenvalues  $(\hbar^2 j_\kappa(j_\kappa + 1))$ ,  $\hbar\mu$ ,  $\hbar^2 l_\kappa(l_\kappa + 1)$ ,  $-\hbar\kappa$ . Once a value of  $\kappa$  is fixed, both  $j_\kappa$  and  $l_\kappa$  are known to be [15]

$$\begin{aligned} l_\kappa &= |\kappa| + \frac{\text{sign}\{\kappa\} - 1}{2}, \\ j_\kappa &= |\kappa| - \frac{1}{2}. \end{aligned} \quad (\text{A3})$$

If one substitutes the expression (A2) into the equation (A1), spin-spherical harmonics cancel out and only radial differential equations remain:

$$\begin{aligned} -\frac{df(r)}{dr} - \frac{1-\kappa}{r}f(r) &= \frac{1}{\hbar c}[E - V(r) - mc^2]g(r), \\ \frac{dg(r)}{dr} + \frac{1+\kappa}{r}g(r) &= \frac{1}{\hbar c}[E - V(r) + mc^2]f(r). \end{aligned} \quad (\text{A4})$$

In terms of

$$u(r) = rg(r); \quad v(r) = rf(r) \quad (\text{A5})$$

one finally gets the radial Dirac equations

$$\begin{aligned} u_\kappa(r) &= -\left(\frac{\hbar c}{\epsilon - V(r)}\right)\left(\frac{d}{dr} - \frac{\kappa}{r}\right)v_\kappa(r), \\ v_\kappa(r) &= \frac{\hbar c}{\epsilon - V(r) + 2mc^2}\left(\frac{d}{dr} + \frac{\kappa}{r}\right)u_\kappa(r), \end{aligned} \quad (\text{A6})$$

where  $\epsilon = E - mc^2$  is the energy of an electron minus its rest mass.

Adopting atomic units, namely,  $\hbar = 1$ ,  $m = 1/2$ ,  $e^2 = 2$ ,  $c = 2/\alpha \sim 274.072$ ,  $\alpha \sim 1/137.037$  (so that lengths are measured in units of  $0.529 \text{ \AA}$  and energies in units of  $13.606 \text{ eV}$ ), the radial Dirac equations (A6) take the form

$$\begin{aligned} u_\kappa(r) &= -\left(\frac{2}{\alpha[\epsilon - V(r)]}\right)\left(\frac{d}{dr} - \frac{\kappa}{r}\right)v_\kappa(r), \\ v_\kappa(r) &= \frac{\alpha}{2} \frac{1}{1 + \frac{\alpha^2}{4}[\epsilon - V(r)]}\left(\frac{d}{dr} + \frac{\kappa}{r}\right)u_\kappa(r), \end{aligned} \quad (\text{A7})$$

where now the electron kinetic energy is  $\epsilon = E - 2/\alpha^2$ .  $u_\kappa(r)$  [or  $g_\kappa(r)$ ] and  $v_\kappa(r)$  [or  $f_\kappa(r)$ ] are called, respectively, *large* and *small* Dirac components, because in the nonrelativistic limit ( $c \rightarrow \infty$ ,  $\alpha \rightarrow 0$ )  $u$  tends to its nonrelativistic Schrödinger model counterpart, while  $v$  simply vanishes.

- 
- [1] J. J. Rehr and R. C. Albers, Theoretical approaches to XAFS, *Rev. Mod. Phys.* **72**, 621 (2000).
- [2] A. Filipponi, A. Di Cicco, and C. R. Natoli, X-ray absorption spectroscopy and n-body distribution functions in condensed matter (I): theory, *Phys. Rev. B* **52**, 15122 (1995).
- [3] A. Filipponi and A. Di Cicco, X-ray absorption spectroscopy and n-body distribution functions in condensed matter (II): data-analysis and applications, *Phys. Rev. B* **52**, 15135 (1995).
- [4] *GNXAS. Extended Suite of Programs for Advanced X-Ray Absorption Data-Analysis: Methodology and Practice*, edited by A. Di Cicco (TASK publishing, Gdansk, Poland, 2009).
- [5] A. Di Cicco, Multiple-edge EXAFS refinement: Short-range structure in liquid and crystalline Sn, *Phys. Rev. B* **53**, 6174 (1996).
- [6] A. Di Cicco, X-ray Absorption Spectroscopy investigations of disordered matter, *Radiat. Phys. Chem.* **175**, 108077 (2020), 17th International Conference on X-ray Absorption Fine Structure- XAFS2018.
- [7] T. A. Tyson, Relativistic effects in the x-ray-absorption fine structure, *Phys. Rev. B* **49**, 12578 (1994).
- [8] A. L. Ankudinov and J. J. Rehr, Relativistic calculations of spin-dependent x-ray-absorption spectra, *Phys. Rev. B* **56**, R1712 (1997).
- [9] J. J. Rehr, J. J. Kas, F. D. Vila, M. P. Prange, and K. Jorissen, Parameter-free calculations of X-ray spectra with FEFF9, *Phys. Chem. Chem. Phys.* **12**, 5503 (2010).
- [10] N. Hara, A. Di Cicco, G. Tchoudinov, K. Hatada, and C. R. Natoli, Relativistic corrections to phase shift calculation in the GNXAS package, *Symmetry* **13**, 1021 (2021).
- [11] C. R. Natoli and D. Sébilleau, Generating phase-shifts and radial integrals for multiple scattering codes, in *Multiple Scattering Theory for Spectroscopies*, edited by D. Sébilleau, K. Hatada, and H. Ebert, Springer Proceedings in Physics Vol. 204 (Springer International Publishing, Cham, 2018), pp. 35–65.
- [12] L. Hedin and B. I. Lundqvist, Explicit local exchange-correlation potentials, *J. Phys. C: Solid State Phys.* **4**, 2064 (1971).
- [13] A. Taranukhina, A. Novakovich, C. R. Natoli, and O. Šipr, Multiple scattering in Green's function formalism: Single-channel and multichannel versions, in *Multiple Scattering Theory for Spectroscopies*, edited by D. Sébilleau, K. Hatada, and H. Ebert, Springer Proceedings in Physics Vol. 204 (Springer International Publishing, Cham, 2018), pp. 171–196.
- [14] J. Zablouil, R. Hammerling, L. Szunyogh, and P. Weinberger, *Electron Scattering in Solid Matter: A Theoretical and Computational Treatise*, Springer Series in Solid-State Sciences Vol. 147 (Springer, Berlin, 2005).
- [15] M. Rose, *Relativistic Electron Theory* (Wiley, New York, 1961).
- [16] J. H. Wood and A. M. Boring, Improved Pauli Hamiltonian for local-potential problems, *Phys. Rev. B* **18**, 2701 (1978).
- [17] C. E. Theodosiou, Lifetimes of alkali-metal—atom Rydberg states, *Phys. Rev. A* **30**, 2881 (1984).
- [18] M. Y. Amusia and L. V. Chernysheva, *Computation of Atomic Processes* (IOP Publishing, London, 1997).
- [19] L. W. Finger, R. M. Hazen, G. Zou, H. K. Mao, and P. M. Bell, Structure and compression of crystalline argon and neon at high pressure and room temperature, *Appl. Phys. Lett.* **39**, 892 (1981).
- [20] C. Hubbard, H. Swanson, and F. Mauer, A silicon powder diffraction standard reference material, *J. Appl. Crystallogr.* **8**, 45 (1975).
- [21] A. W. Hull, The crystal structure of calcium, *Phys. Rev.* **17**, 42 (1921).
- [22] E. R. Jette and F. Foote, Precision determination of lattice constants, *J. Chem. Phys.* **3**, 605 (1935).
- [23] P. D'Angelo, A. Di Cicco, A. Filipponi, and N. V. Pavel, Double-electron excitation channels at the Br K-edge of HBr and Br<sub>2</sub>, *Phys. Rev. A* **47**, 2055 (1993).
- [24] B. Olinger and J. C. Jamieson, Zirconium: Phases and compressibility to 120 kilobars, *High Temp. High Press.* **5**, 123 (1973).
- [25] N. Ridley, Densities of some indium solid solutions, *J. Less-Common Met.* **8**, 354 (1965).

- [26] F. H. Spedding, A. H. Daane, and K. W. Herrmann, Electrical resistivities and phase transformations of lanthanum, cerium, praseodymium, and neodymium, *JOM* **9**, 895 (1957).
- [27] I. Harris and G. Raynor, Some observations on the crystal structures of the rare-earth metals and alloys, *J. Less-Common Met.* **17**, 336 (1969).
- [28] A. Maeland and T. B. Flanagan, Lattice spacing of gold-palladium alloys, *Can. J. Phys.* **42**, 2364 (1964).
- [29] A. Di Cicco, M. Minicucci, E. Principi, A. Witkowska, J. Rybicki, and R. Laskowski, Testing interaction models by using x-ray absorption spectroscopy: solid Pb, *J. Phys.: Condens. Matter* **14**, 3365 (2002).
- [30] D. Evans and G. Raynor, The lattice spacing of thorium, with reference to contamination, *J. Nucl. Mater.* **1**, 281 (1959).
- [31] M. O. Krause and J. H. Oliver, Natural widths of atomic K and L levels, K alpha X-ray lines and several KLL Auger lines, *J. Phys. Chem. Ref. Data* **8**, 329 (1979).
- [32] J. G. Norman, Non-empirical versus empirical choices for overlapping-sphere radii ratios in SCF- $X_\alpha$ -SW calculations on  $\text{ClO}_4^-$  and  $\text{SO}_2$ , *Mol. Phys.* **31**, 1191 (1976).
- [33] P. Schwerdtfeger, *Relativistic Electronic Structure Theory. Part 2. Applications* (Elsevier, Amsterdam, 2004).
- [34] P. Pyykko, Relativistic effects in structural chemistry, *Chem. Rev.* **88**, 563 (1988).
- [35] R. E. Benfield, A. Filipponi, D. T. Bowron, R. J. Newport, and S. J. Gurman, An X-ray absorption study of gold coordination compounds: EXAFS refinements and double electron excitation background, *J. Phys.: Condens. Matter* **6**, 8429 (1994).
- [36] A. Di Cicco and A. Filipponi, Evidence for [2p(s)4f] multi-electron resonances in x-ray-absorption spectra of sixth-period elements, *Phys. Rev. B* **49**, 12564 (1994).
- [37] M. A. Karolewski, R. G. Cavell, R. A. Gordon, C. J. Glover, M. Cheah, and M. C. Ridgway, Predicting XAFS scattering path cumulants and XAFS spectra for metals (Cu, Ni, Fe, Ti, Au) using molecular dynamics simulations, *J. Synchrotron Radiat.* **20**, 555 (2013).
- [38] T. Comaschi, A. Balerna, and S. Mobilio, Temperature dependence of the structural parameters of gold nanoparticles investigated with EXAFS, *Phys. Rev. B* **77**, 075432 (2008).
- [39] M. G. Pamato, I. G. Wood, D. P. Dobson, S. A. Hunt, and L. Vočadlo, The thermal expansion of gold: point defect concentrations and pre-melting in a face-centred cubic metal, *J. Appl. Crystallogr.* **51**, 470 (2018).
- [40] A. Filipponi and A. Di Cicco, Short-range order in crystalline, amorphous, liquid, and supercooled germanium probed by x-ray absorption spectroscopy, *Phys. Rev. B* **51**, 12322 (1995).
- [41] E. Sevillano, H. Meuth, and J. J. Rehr, Extended x-ray absorption fine structure Debye-Waller factors. I. Monatomic crystals, *Phys. Rev. B* **20**, 4908 (1979).
- [42] J. J. Sakurai, *Advanced Quantum Mechanics* (Addison-Wesley, Boston, 1967).